PNAS RESEARCH ARTICLE | APPLIED PHYSICAL SCIENCES OPEN ACCESS

A frictional soliton controls the resistance law of shear-thickening suspensions in pipes

Alexis Bougouin[a], Bloen Metzger[a], Yoël Forterre[a], Pascal Boustingorry[b], and Henri Lhuissier[a,1]

Edited by David Weitz, Harvard University, Cambridge, MA; received December 8, 2023; accepted March 14, 2024

Pipe flows are commonly found in nature and industry as an effective mean of transporting fluids. They are primarily characterized by their resistance law, which relates the mean flow rate to the driving pressure gradient. Since Poiseuille and Hagen, various flow regimes and fluid rheologies have been investigated, but the behavior of shear-thickening suspensions, which jam above a critical shear stress, remains poorly understood despite important applications (e.g., concrete or food processing). In this study, we build on recent advances in the physics of shear-thickening suspensions to address their flow through pipes and establish their resistance law. We find that for discontinuously shear-thickening suspensions (large particule volume fractions), the flow rate saturates at high driving stress. Local pressure and velocity measurements reveal that this saturation stems from the emergence of a frictional soliton: a unique, localized, superdissipative, and backpropagating flow structure coexisting with the laminar frictionless flow phase observed at low driving stress. We characterize the remarkably steep effective rheology of the frictional soliton and show that it sets the resistance law at the whole pipe scale. These findings offer an unusual perspective on low-Reynolds suspension flows through pipes, intriguingly reminiscent of the transition to turbulence for simple fluids. They also provide a predictive law for the transport of such suspensions in pipe systems, with implications for a wide range of applications.

pipe flow | shear-thickening suspension | jamming | soliton | friction

Significance

Pipe flow is an emblematic configuration in fluid mechanics, the basis for describing the laminar/turbulent transition, and a widespread fluid transport mode in nature and industry. Yet, it is still not known how a suspension of small particles, which shear-thickens and jams, can flow in such a confined space. We show here that it does so by nucleating a superdissipative local flow structure: a frictional soliton, which acts as a sharp flow-limiter, governing the global resistance law of the pipe. These results uncover a highly unconventional picture of viscous (low Reynolds number) pipe flows—a foundational step in improving many industrial processes.

In 1840, Poiseuille and Hagen (1–3) established experimentally the laminar resistance law for a Newtonian liquid, $Q \propto -R^4 \nabla P/\eta_l$, by which the volume flow rate Q increases with pipe radius R and pressure gradient ∇P, and decreases with liquid viscosity η_l. Since then, a vast literature initiated by Reynolds (4) has documented the limit of this laminar regime, beyond which, inertial eddying flow structures (turbulent puffs and slugs) form and the hydraulic resistance starts deviating from Poiseuille law (5–10). Investigations have also concerned more complex materials (elasto-visco-plastic fluids or particulate suspensions), for which the effective rheology or interphase flow may modulate Poiseuille law (11–14) or alter the transition to turbulence (15–19). By contrast, the case of shear-thickening suspensions has received much less attention (20), and it is still unclear how these suspensions flow through pipes, even though they are frequently encountered in industry, from high-performance concretes (21) to food (22), and in nature, from diseased blood (23) to crystal-rich lava (24, 25).

The problem is rather general since most suspensions of small (∼5 to 50 μm) nonaggregating particles actually show a steep shear-thickening behavior controlled by the shear stress level. At sufficiently large particle volume fractions, these suspensions flow under a mild stress, but discontinuously shear-thicken or jam, above a critical stress. This peculiar rheology has been shown to stem from a change in the effective friction coefficient between particles, as their mutual repulsive force is overcome (26–28). On a macroscopic scale, it has also been shown to promote new flow instabilities (29–34), complex transient flow structures (35–39), and nontrivial drag laws (40, 41), in a few common flows (in Couette cells, down inclines, or past cylinders). These jamming structures raise questions about how shear-thickening suspensions can actually flow in highly confined wall-bounded configurations. In particular, it is currently not known how they flow through a pipe, where bulk incompressibility imposes uniformity of the flow rate along the pipe.

The present work tackles this question on experimental grounds. We use a gravitational pipe drainage protocol offering a precise control on the key parameter of the flow: the mean shear stress at the wall. Near-wall visualizations combined with local and global hydraulic resistance measurements reveal the fascinating way by which the flow proceeds: At high stress, the flow nucleates a solitary backpropagating flow phase, with a

Author affiliations: [a]Aix Marseille Univ, CNRS, Institut Universitaire des Systèmes Thermiques et Industriels, Marseille 13453, France; and [b]Chryso France, Sermaises 45300, France

Author contributions: A.B., B.M., Y.F., P.B., and H.L. designed research; performed research; analyzed data; and wrote the paper.

The authors declare no competing interest.

This article is a PNAS Direct Submission.

[1]To whom correspondence may be addressed. Email: henri.lhuissier@univ-amu.fr.

This article contains supporting information online at https://www.pnas.org/lookup/suppl/doi:10.1073/pnas.2321581121/-/DCSupplemental.

Published April 16, 2024.

plug-like velocity profile. We characterize the flow bifurcation, identify the frictional and superdissipative nature of the soliton, and show how it sets the resistance law of the suspension along the whole pipe. Last, we address the universality of the phenomenology for discontinuously shear-thickening suspensions and discuss the mechanism behind the superdissipation.

Results

Experimental Set-Up. To study the intrinsic pipe flow, without pumping fluctuations or entrance effects, we use the configuration sketched in Fig. 1*A*: the gravitational drainage of a long inclined pipe, initially filled with a shear-thickening suspension (see *M&M* for details on setup, materials or protocol). This configuration has two crucial advantages. i) It avoids convergent/divergent flow sections (20), which could localize stresses and trigger jamming (see experiments and discussion on convergent inlet in *SI Appendix*, SI.2). ii) Gravity ensures a steady and controllable average forcing of the flow. Indeed, since inertial effects are small (Reynolds number $\lesssim 10$ with slowly varying flow), the force balance over the flow length L implies that the mean shear stress at the wall $\langle\tau_w\rangle \equiv \frac{1}{L}\int_0^L \tau_w \mathrm{d}x = \rho g R \sin\theta/2$ is constant for the whole drainage and is simply set by the suspension density ρ, gravity g, the inner pipe radius R and the pipe inclination θ (Fig. 1 *A*, *Inset*).

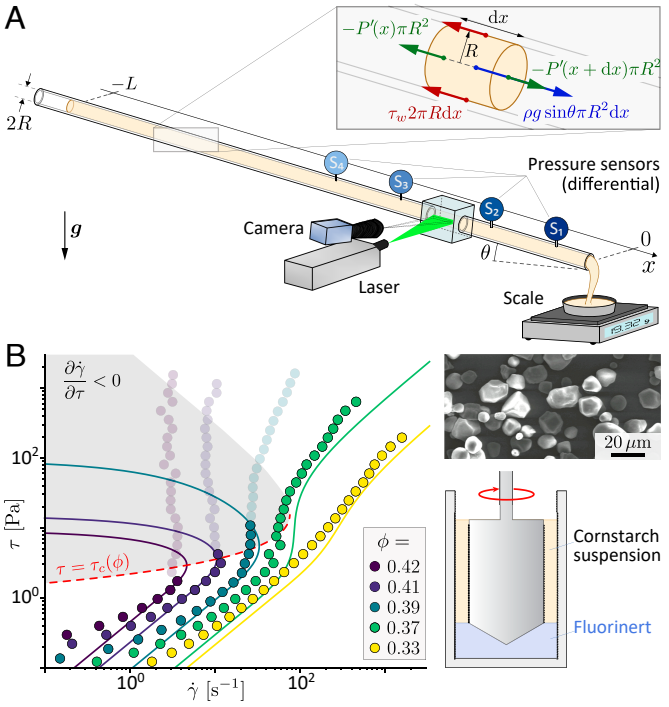

Fig. 1. (*A*) Sketch of the gravity-driven setup allowing to control the mean wall shear stress $\langle\tau_w\rangle$ through pipe inclination, measure global flow rate and local bulk pressure, and visualize near-wall flow. (*Inset*) Force balance on a slice of suspension. (*B*) Suspension rheology (70): shear stress versus shear rate for aqueous suspensions of cornstarch grains (optical microscope image) at various solid volume fractions ϕ obtained with a cylindrical Couette cell (sketch). Solid lines: fit to Wyart–Cates rheological model $\tau = \eta_S(\phi_0 - (\phi_0-\phi_1)\mathrm{e}^{-\tau^*/\tau} - \phi)^{-2}\dot\gamma$ setting the viscosity prefactor $\eta_S = 0.28$ mPa s, the frictionless and frictional jamming volume fractions $\phi_0 = 0.445$ and $\phi_1 = 0.385$, respectively, and the short-range repulsive stress scale $\tau^* = 8$ Pa (semitransparent symbols are not used to fit). Red dashed line: critical stress $\tau_c(\phi)$ at which Wyart–Cates curves become negatively sloped ($\partial\dot\gamma/\partial\tau < 0$, gray region).

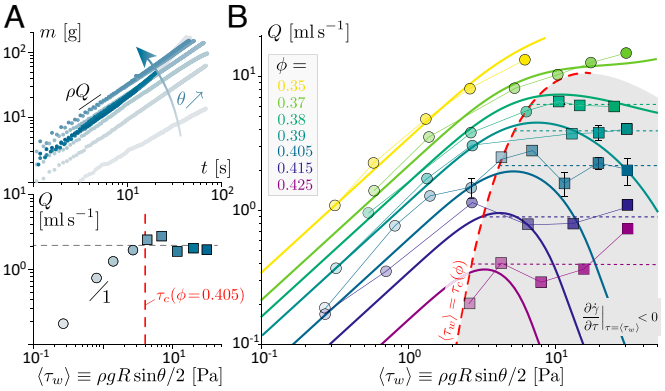

Fig. 2. Global resistance law (70). (*A*) *Top*: drained mass of suspension vs time for fixed volume fraction ($\phi = 0.405 > \phi_{\mathrm{DST}}$) and increasing pipe inclination. *Bottom*: corresponding flow rate Q vs mean wall stress. (*B*) Q for various volume fractions. Red dashed line: flow rate saturation onset criterion $\langle\tau_w\rangle = \tau_c(\phi)$, for the Wyart–Cates rheological laws fitted in Fig. 1*B*. Dashed lines: experimental average highlighting flow rate saturation in the gray region (where $\partial\dot\gamma/\partial\tau|_{\tau=\langle\tau_w\rangle} < 0$, for a laminar flow). Solid lines: flow rate expected for a steady laminar flow (see also *SI Appendix*, SI.3). Symbol shape indicates experimental observation of the laminar phase only (○) or laminar phase + frictional soliton (□). $R = 5.15$ mm in (*A*) and (*B*).

Most experiments are performed with an aqueous suspension of cornstarch grains (Fig. 1*B* image). This widely documented system is known for its marked discontinuous shear-thickening rheology, which we characterize at different solid volume fractions ϕ with a Couette cell apparatus (other particles are used to verify that results are generic of shear-thickening suspensions, see below and *M&M*). Rheograms are fitted with Wyart–Cates model (27) (solid lines in Fig. 1*B*) to obtain the low-stress (frictionless) viscosity $\eta_0(\phi) = \eta_S(\phi_0 - \phi)^{-2}$ and the critical shear stress $\tau_c(\phi) \equiv \tau|_{\partial\dot\gamma/\partial\tau=0}$ (red dashed line), above which suspensions with a sufficiently high particle volume fraction ($\phi > \phi_{\mathrm{DST}} \approx 0.37$) show a discontinuous shear-thickening (see caption of Fig. 1 for the definition of η_S and ϕ_0).

Saturation of the Flow Rate. We investigate, first, the global resistance law of the pipe, i.e., the evolution of the flow rate with the forcing, starting with a discontinuously shear-thickening suspension ($\phi = 0.405 > \phi_{\mathrm{DST}}$). The forcing $\langle\tau_w\rangle$ is varied through the pipe inclination and flow rate is obtained by weighing the drained suspension at the pipe outlet (Fig. 1*A*). As shown in Fig. 2*A*, the drained mass m increases linearly with time over the whole range of inclination $0.5° < \theta < 90°$ (i.e., $0.27\,\mathrm{Pa} \leq \langle\tau_w\rangle \leq 31\,\mathrm{Pa}$), which indicates the flow rate $Q \equiv \dot m/\rho$ does not vary during drainage. However, Q depends on inclination, with two strikingly different trends. At low forcing ($\langle\tau_w\rangle \lesssim 4$ Pa), flow rate increases quasi-linearly with $\langle\tau_w\rangle$, as for the laminar flow of a Newtonian liquid. By contrast, for higher forcings ($\langle\tau_w\rangle \gtrsim 4$ Pa), the flow rate is found to saturate: the same value ($Q \approx 1.8$ ml/s) is obtained over a more than 10-fold increase in the forcing. Notably, the mean wall stress at the onset of saturation closely matches the discontinuous shear-thickening onset stress $\tau_c(\phi = 0.405) \approx 4.0$, as obtained from the rheological characterization (Fig. 1*B*).

To confirm and generalize these two global responses of the flow, we extend experiments to a wide range of particle volume fraction ($0.35 \leq \phi \leq 0.425$) and recover that flow rate saturates at high forcings ($\langle\tau_w\rangle > \tau_c(\phi)$), provided volume fraction is sufficiently high ($\phi > \phi_{\mathrm{DST}}$). The region of flow rate saturation (highlighted with horizontal lines) coincides with the region where $\partial\dot\gamma/\partial\tau|_{\tau=\langle\tau_w\rangle} < 0$ (highlighted in gray). This confirms

that flow rate saturation is triggered by the discontinuous shear-thickening of the suspension at the pipe wall, where the shear stress is maximal for a laminar flow.

This indicates that available S-shape rheological models, which capture the dependence of τ_c with ϕ, are sufficient to capture the onset of flow rate saturation. However, such models do not explain, alone, why and how the flow saturates. Indeed, the base-state flow rate predicted from these rheological laws for a steady laminar flow does not plateau but, actually, decreases strongly at high forcings (see solid lines in Fig. 2*B*, and *SI Appendix*, SI.3, for the derivation). Therefore, additional information on the structure of the flow is needed to elucidate the mechanism behind flow rate saturation.

Evidence of a Localized Flow Structure: The Frictional Soliton. To obtain such information we use a transparent pipe, seed the suspension with fluorescent tracers, shine a laser sheet through the wall and optically monitor the flow over a $\sim 8R$-long pipe section located $\approx$40 cm upstream the pipe outlet (see Fig. 1*A*, *SI Appendix*, Movies in SI.1 and more details on optical measurements in *M&M*). Given the suspension opacity, light only penetrates a thin layer of suspension (with an estimated thickness $\sim$100 μm, see *SI Appendix*, SI.4), which gives access to the near-wall velocity of the suspension (see sketches in Fig. 3 *A* and *B*).

As shown in Fig. 3, the spatiotemporal evolution of the near-wall flow differs qualitatively between the low and high-forcing regimes. For low forcings ($\langle\tau_w\rangle < \tau_c(\phi)$, Fig. 3*A*, *SI Appendix*, SI.1 Movie S1), the near-wall flow is uniform and steady, which is consistent with a Poiseuille-like laminar flow in the pipe, as expected from the quasi-Newtonian behavior of the suspension at low stresses. The mean near-wall velocity $U_w \approx 0.10U$ (averaged over the observation depth, see *SI Appendix*, SI.4), is approximatively one decade smaller than the mean-flow velocity $U = Q/\pi R^2$. By contrast, at high forcings ($\langle\tau_w\rangle > \tau_c(\phi)$, Fig. 3*B*, *SI Appendix*, SI.1 and Movie S2) the near-wall flow reveals an intriguing flow structure. While the near-wall flow (within the camera field of view) is initially steady and uniform, as in the low forcing regime, a short, nonsteady, nonuniform region is observed, which propagates upstream with a constant velocity c and a preserved length ℓ, before the flow returns to its previous laminar (frictionless) state. This reveals that flow rate saturation is associated with the inception of a new flow phase: a localized, purely propagative structure, which we call frictional soliton.

Near-wall velocimetry also provides information on the cross-sectional velocity profile within the different flow phases. Upstream and downstream from the soliton, the near-wall velocity ($U_w \approx 0.06U$ and $0.13U$, respectively) remains one order of magnitude below the mean velocity U, which suggests the flow profile is Poiseuille-like, as in the low-forcing regime. However, in the frictional soliton, the near-wall velocity $U_w^{FS} \approx 0.6U$ has typically the same magnitude as U, which suggests a velocity profile closer to a plug flow, as schematized in Fig. 3*B* (additional measurements of the velocity variations across the near-wall observation depth also suggests a finite slip velocity at the wall, see details in *SI Appendix*, SI.4).

To document the soliton characteristics and their dependence to the suspension and flow conditions, we perform systematic near-wall observations, for varied flow forcings, particle volume fractions, and pipe radii. Measurements (Fig. 3*C*) reveal that the length $\ell = (1.5 \pm 0.5)2R$ of the soliton is essentially set by the local length scale of the pipe, namely its diameter $2R$ with, however, a mild trend toward shorter solitons close to the onset forcing ($\langle\tau_w\rangle \lesssim 3\tau_c$), where solitons are sometimes found to be evanescent. Moreover, the (upstream) propagation velocity of the soliton, $c = (1.5 \pm 1)U$, is found to be of the order of the mean flow velocity, regardless of applied stress or particle volume fraction. This suggests a different mechanism from those reported for shear-jamming fronts (35, 42–44), whose propagation velocity is typically one order of magnitude larger than the flow velocity and strongly depends on volume fraction.

A crucial piece of information about the frictional soliton is also provided by observing microscopic air bubbles, which are seldomly and fortuitously trapped in the suspension. Fig. 3*D* shows the behavior of such bubbles as the frictional soliton passes. Upstream of the soliton, bubbles (tiny white spots) have a stable size of approximately 20 μm. Within the soliton, however, they

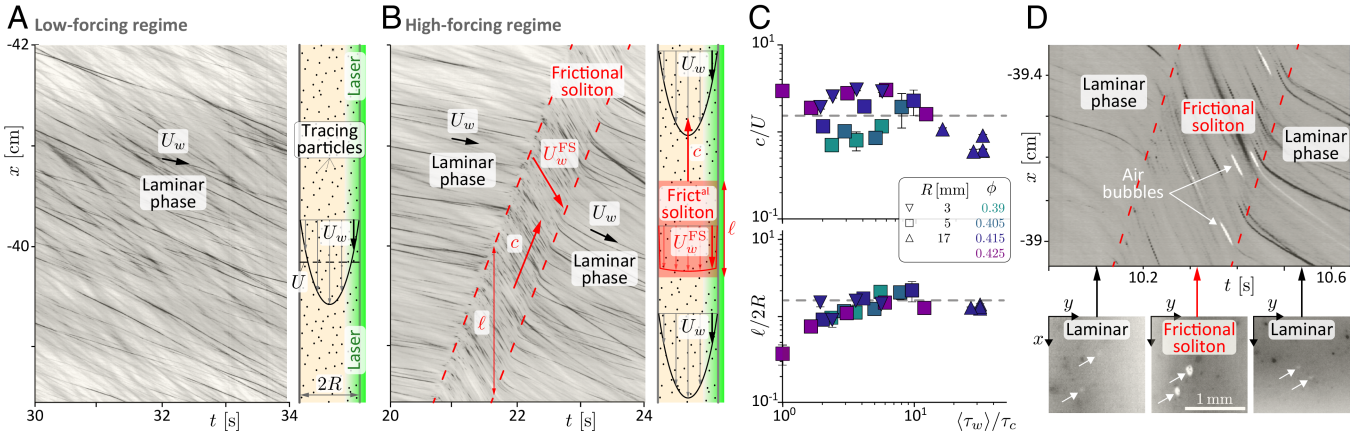

Fig. 3. Identification of the frictional soliton. (*A* and *B*) Spatiotemporal images of the near-wall flow along a pipe generatrix, at $\approx$40 cm upstream the pipe outlet ($\phi = 0.405 > \phi_{DST}$, $R = 5.15$ mm, see *SI Appendix*, Movies in SI.1). The (x, t) trajectory of the tracing particles (black) indicates the near-wall velocity U_W [different velocities at a given (x, t) reflect different distances of the tracing particles to the wall]. (*A*) At low forcing ($\theta = 4.9°$, $\langle\tau_W\rangle = 2.6$ Pa $< \tau_c$), a single laminar phase of steady, uniform and low near-wall velocity is observed ($U_W \approx 0.10U$). (*B*) At large forcing ($\theta = 22.0°$, $\langle\tau_W\rangle = 11.6$ Pa $> \tau_c$), a localized frictional-soliton phase of high wall-velocity ($U_W \approx 0.6U$) separates two laminar phases and propagates against the flow. Sketches: Inferred velocity profiles in the laminar and frictional-soliton phases. (*C*) Scaled velocity and width of the soliton vs scaled mean wall stress (70). The dashed lines are $c/U = 1.5$ and $\ell/2R = 1.5$. (*D*) *Top*: Spatiotemporal image of the near-wall flow highlighting the liquid pressure drop in the frictional soliton through the expansion of small probe air bubbles (white) transported by the suspension ($\phi = 0.39$, see *SI Appendix*, Movie in SI.1). *Bottom*: Snapshot images showing the same two bubbles upstream (*Left*), inside (*Middle*), and downstream (*Right*) the soliton.

grow notably, increasing their diameter by a factor 2 to 4, before collapsing back to their original size once the soliton has passed. This transient expansion of the bubbles reveals a pressure drop in the liquid of the suspension, inside the soliton. This pore pressure drop actually reflects a symmetric increase in the particulate pressure, i.e., the pressure supported by contacts between grains and between grains and the pipe wall (45–49). The magnitude of the bubbles expansion (1 to 2 decades in volume) suggests a pore pressure drop by typically one atmosphere or more (see details in *SI Appendix*, SI.5), i.e., a massive increase in the granular pressure at the wall, which controls the shear stress of the suspension. This observation suggests that the frictional soliton is the locus of a strong resistance to the flow, which calls for a more direct estimation of the stress distribution along the pipe.

The Frictional Soliton Is a Superdissipative Structure. To obtain the evolution of the wall stress along the pipe, the bulk pressure P' (relative to ambient) is measured at several distances from the pipe outlet (see Fig. 1*A* and *M&M*). In the presence of pressure gradients and neglecting inertia, the force balance on a slice of suspension gives $\tau_w = -(R/2)\nabla(P' + \rho g z)$, with τ_w the local wall stress and $z = -\sin\theta x$ the elevation relative to the pipe outlet. Fig. 4 presents the evolution of the reconstructed total pressure, $P = P' + \rho g z$, which quantifies the loss between the current abscissa x and the pipe outlet, together with the time evolution of the suspension surface position $-L$. For low forcings ($\langle\tau_w\rangle < \tau_c(\phi)$, Fig. 4*A*), P is fixed in time at each sensor, and values from different sensors show a linear decrease along the pipe. These measurements confirm the steadiness and uniformity of the flow, and imply that the assessed local wall stress τ_w is uniform and equal to $\langle\tau_w\rangle$ (see profile of P at 30 s).

For high forcings, ($\langle\tau_w\rangle > \tau_c(\phi)$, Fig. 4*B*), the frictional soliton changes the evolution of the total pressure P qualitatively. Let us consider, first, the temporal evolution for a fixed position; that of the most downstream sensor S_1. At flow start ($t = 0$), P is much higher than expected for a uniform resistance (≈0.5 kPa, dark blue dashed line), which indicates a large overdissipation downstream. At $t \approx 5$ s, the pressure P suddenly drops to a fraction of the uniform-flow expectation (dark blue dashed line), signaling that the overdissipation has moved upstream of sensor S_1 within a very short time ($t_{\text{drop}} \approx 0.4$ s). Subsequently, P remains essentially constant for a long period ($t \lesssim 44$ s), reflecting steady losses downstream. A similar signal is obtained at sensors S_2, S_3, and S_4, albeit for the delay before pressure drop, which increases linearly with sensor distance to the pipe outlet. These sudden pressure drops are found to be exactly synchronous with the passage of the frictional soliton, as inferred from the passing time and velocity measured by near-wall flow observations between S_2 and S_3. This reveals that the frictional soliton is the locus of a superdissipation, since local (bulk) pressure drop directly reflects local dissipation (given the constant flow rate and negligible inertia). Wall stress is highly increased within a short length $\ell_{\text{drop}} \equiv ct_{\text{drop}} \approx 1.4R$, of order the soliton length $\ell \approx 3R$ identified from near-wall velocimetry (Fig. 3*C*). The typical magnitude of the local wall stress can be inferred from the pressure drop across the soliton, $\Delta P_{\text{drop}} \sim 5$ kPa, and the length ℓ_{drop} according to $\tau_w \sim R\Delta P_{\text{drop}}/2\ell_{\text{drop}} \sim 2$ kPa, i.e., $\tau_w \sim 10^2\langle\tau_w\rangle$. Conversely, upstream and downstream, wall stress is uniform and steady. Measurements reveal a constant substress $\tau_w \approx 3.3$ Pa ($< \langle\tau_w\rangle = 11.6$ Pa), which actually compares with the critical shear stress of the suspension $\tau_c \approx 4.0$ Pa (see profile of P at 25 s).

Additionally, the extrapolation of the soliton trajectory intersects $x = 0$ at $t = 0$, indicating that the soliton nucleates at the pipe outlet when flow starts (see Fig. 4 *B*, *Left* and *M&M*). Crucially, when the soliton reaches the upper surface of the suspension (intersect of red and green trajectories in Fig. 4 *B*, *Left*), the total pressures of the four sensors step back, synchronously, to a large value, signaling the inception of a new soliton at the pipe outlet, at the instant the first one extinguishes. This indicates that a single soliton is actually maintained to accommodate the high forcing. Last, a slight increase in the flow rate, by a typical factor 2, is observed as the second soliton replaces the first one, which suggests that the passage of the first soliton somehow modifies the distribution or structure of the suspension grains (as a reference, no change in flow rate is observed for the same drained mass in the low forcing regime, Fig. 4*A*).

Altogether, these measurements highlight that flow rate saturation at high forcings is the consequence of the inception and self-preserving upstream propagation of a single, localized, and superdissipative flow structure: a frictional soliton. The localization of high stresses in the soliton actually allows the rest of the suspension, both upstream and downstream, to sustain only a mild stress $\sim\tau_c$, compatible with the frictionless state, hence, a laminar flow.

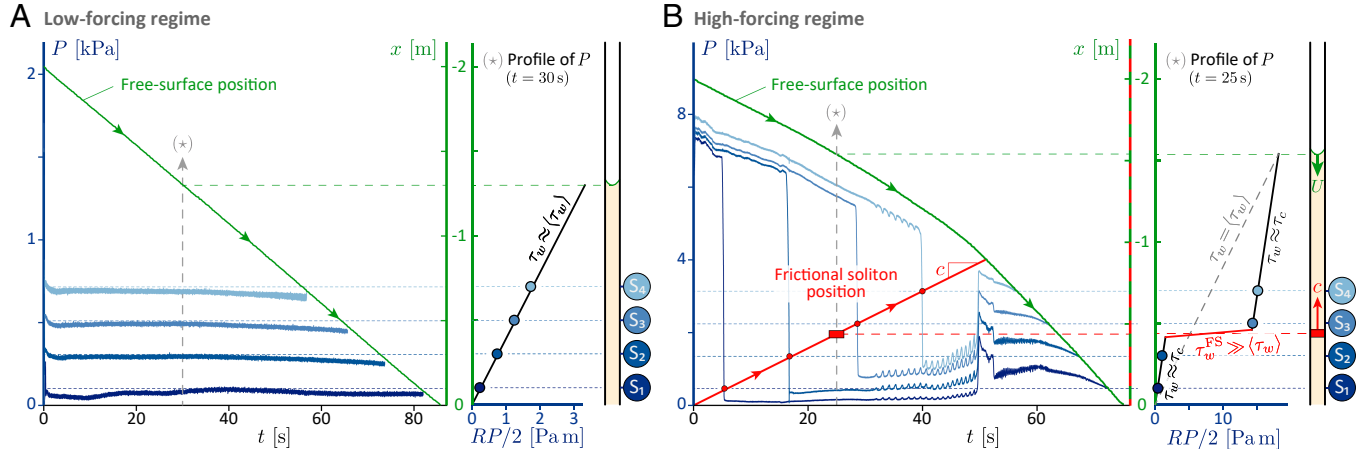

Fig. 4. Dissipation along the pipe (70). (*A* and *B*, *Left*) Temporal evolution of the total flow pressure $P = P' - \rho g \sin\theta x$ at sections S_1 to S_4 (blue curves) for $\phi = 0.405 > \phi_{\text{DST}}$ ($R = 5.15$ mm). (*A*) Low-forcing regime ($\theta = 4.9°$, $\langle\tau_w\rangle = 2.6$ Pa $< \tau_c$). (*B*) High-forcing regime ($\theta = 22.0°$, $\langle\tau_w\rangle = 11.6$ Pa $> \tau_c$). Green line: free-surface position (inferred from drained suspension mass). Blue dashed lines: expected values of P for a steady uniform flow. Red line in (*B*): frictional-soliton position (red circles mark passing times at S_1 to S_4, the line is a linear fit). (*A* and *B*, *Right*) Inferred longitudinal profile of $RP/2$ (at fixed time). The inverse slope $\tau_w \equiv -R\nabla P/2$ is the local wall stress.

Two-Flow-Phase Model of the High-Forcing Regime. The observations reported above allow to envision the high-forcing regime as the coexistence of two flow phases, providing guides for establishing quantitative local resistance laws for all flow regimes and phases. In the low-forcing regime ($\langle\tau_w\rangle \lesssim \tau_c(\phi)$), the steady and uniform resistance is simply $\langle\tau_w\rangle$. In the high-forcing regime ($\langle\tau_w\rangle \gtrsim \tau_c(\phi)$), the resistance of the laminar phase is close to the critical stress $\tau_c(\phi)$, whereas the frictional-soliton phase carries the global load $2\pi RL\langle\tau_w\rangle$ minus the part $\approx 2\pi R(L-\ell)\tau_c(\phi)$ taken by the laminar phase. This can be summarized with the following laws, valid at resolution down to the cross-sectional scale R:

Low-forcing regime $(\langle\tau_w\rangle < \tau_c(\phi))$

$$\tau_w = \langle\tau_w\rangle, \qquad \text{everywhere.} \qquad [1]$$

High-forcing regime $(\langle\tau_w\rangle > \tau_c(\phi))$

$$\tau_w \approx \begin{cases} \tau_c(\phi), & \text{in the laminar phase,} \\ \tau_c(\phi) + \frac{L}{\ell}(\langle\tau_w\rangle - \tau_c(\phi)), & \text{in the soliton phase.} \end{cases} \qquad [2]$$

These laws can be tested against experiments. Fig. 5*A* presents systematic measurements of the local wall stress, $\tau_w \equiv -R\nabla P/2$, as inferred from the pressure measurements along the pipe (see Fig. 5 caption). At low forcings ($\langle\tau_w\rangle < \tau_c(\phi)$), the local wall stress τ_w matches the mean imposed stress $\langle\tau_w\rangle$ in agreement with Eq. **1**. For high forcings ($\langle\tau_w\rangle > \tau_c(\phi)$), the local wall stress strongly depends on the flow phase. In the laminar phase (yellow and orange squares) the wall stress is close to the critical stress ($\tau_w \approx \tau_c(\phi)$), independently of the average forcing $\langle\tau_w\rangle$ and of the flow length L, consistently with Eq. **2**. By contrast, the local wall stress measured in the soliton phase (red and pink squares) is much larger and depends on both quantities. For a fixed flow length L, it increases linearly with the excess forcing $\langle\tau_w\rangle - \tau_c$, as anticipated by Eq. **2**. The agreement is not only observed up to the largest gravitational forcing $\langle\tau_w\rangle = \rho g R/2 \approx 8\tau_c$ obtained for a vertical pipe, but also for a higher forcing $\langle\tau_w\rangle \approx 26\tau_c$ (stroked red square in Fig. 5*A*) obtained by imposing an additional pressure difference between the top and bottom of the pipe, using pressurized air. The resistance also follows the linear trend in the flow length L of Eq. **2**, as verified by using a ten times shorter pipe (pink squares in Fig. 5*A*).

Importantly, if the local resistance laws give information on the stress with a resolution down to the pipe radius—which is useful to address the load and fatigue on the pipe structure down to this scale—they also embed the global resistance law of the flow. Indeed, the pipe always contains a laminar phase, with a wall stress following $\tau_w \approx \frac{4\eta_0}{\pi R^3}Q$, up to the critical flow rate $Q_c \equiv \frac{\pi R^3}{4\eta_0}\tau_c(\phi)$ obtained at $\langle\tau_w\rangle \approx \tau_c(\phi)$. Integrating Eqs. **1** and **2** along the pipe thus yields:

Low-forcing regime $(\langle\tau_w\rangle < \tau_c(\phi))$

$$Q \approx \frac{\pi R^3}{4\eta_0}\langle\tau_w\rangle, \qquad [3]$$

High-forcing regime $(\langle\tau_w\rangle > \tau_c(\phi))$

$$Q \approx \frac{\pi R^3}{4\eta_0}\tau_c(\phi) \equiv Q_c(\phi, R), \qquad [4]$$

which is the global flow curve discussed in Fig. 2, with a linear increase at low-forcing and a saturation at high-forcing. Notably, Eq. **3** is experimentally verified for varied pipe radii ($R \approx 3$, 5, and 17 mm, see *SI Appendix*, SI.6). Therefore, flow saturates at highly different Reynolds numbers, including values much below 1 ($\rho Q/\pi\eta_0 R \approx 0.04 - 7$), which indicates that flow saturation is not of inertial origin but stems from the specific rheological response of the suspension to the flow.

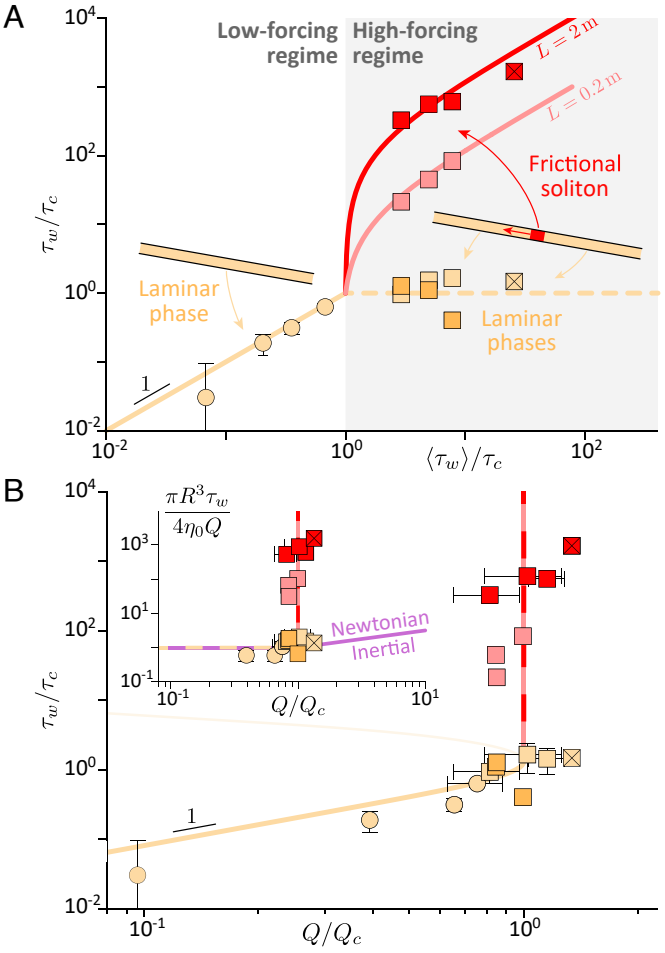

Fig. 5. Local resistance law of the laminar and soliton phases (70) ($\phi = 0.405$). (*A*) Local wall stress vs mean applied wall stress (both scaled by the critical shear stress τ_c measured in Fig. 1*B*). Yellow lines: Eq. **1** (solid) and laminar branch of Eq. **2** (dashed). Red and pink lines: frictional-soliton branch of Eq. **2**, for different initial flow length ($L = 0.2$ and 2 m). (*B*) Local wall stress vs scaled flow rate ($Q_c \equiv \pi R^3\tau_c/4\eta_0$, with values of η_0 and τ_c obtained in Fig. 1*B*). Yellow line: base-state expectation from the Wyart–Cates rheological law. Red-pink dashed line: Eq. **4**. (*A* and *B*) Symbol color refers to $L = 2$ m (red, yellow) and $L = 0.2$ m (pink, orange). Symbol shape indicates laminar phase only (○), or laminar phase + frictional soliton (□; ⊠ indicates $\langle\tau_w\rangle$ is imposed by gravity + air pressure difference, see text; the wall stress in the soliton is obtained from the pressure drop across the pipe portion containing the soliton and by subtracting the laminar contribution over the length $S_iS_{i+1} - \ell$; vertical error bars indicate the SD between measurements over S_1S_2, S_2S_3, and S_3S_4). (*Inset*) Same data nondimensionalized by the laminar stress $\frac{4\eta_0 Q}{\pi R^3}$ highlighting the functional difference between the frictional-soliton bifurcation (symbols, yellow and red-pink lines, Eqs. **1** and **2** with $Q_c = \pi R^3\tau_c(\phi)/4\eta_0$) and the inertial transition of a Newtonian liquid [purple line, $\frac{\pi R^3\tau_w}{4\eta_0 Q} \approx \left(\frac{Q}{Q_c}\right)^{1/4}$ with $Q_c \approx \left(\frac{64}{0.3164}\right)^{4/3}\frac{\pi\eta_0 R}{\rho}$ (9)].

Last, it must be realized that the local resistance law of the soliton phase (Eq. **2**) is of a very peculiar kind and actually reveals a singularly steep rheology. This is highlighted in Fig. 5*B*, by presenting the evolution of the local wall stress τ_w with the pipe flow rate Q. At low flow rates ($Q < Q_c$), the flow is in the laminar regime and local stresses follow the global forcing, as already discussed in Figs. 2*C* and 5*A*. However, close to Q_c, a frictional soliton forms and the wall stress in the soliton shows a very steep increase (red-pink dashed line), which reflects that the frictional soliton actually behaves as a sharp flow rate limiter: it

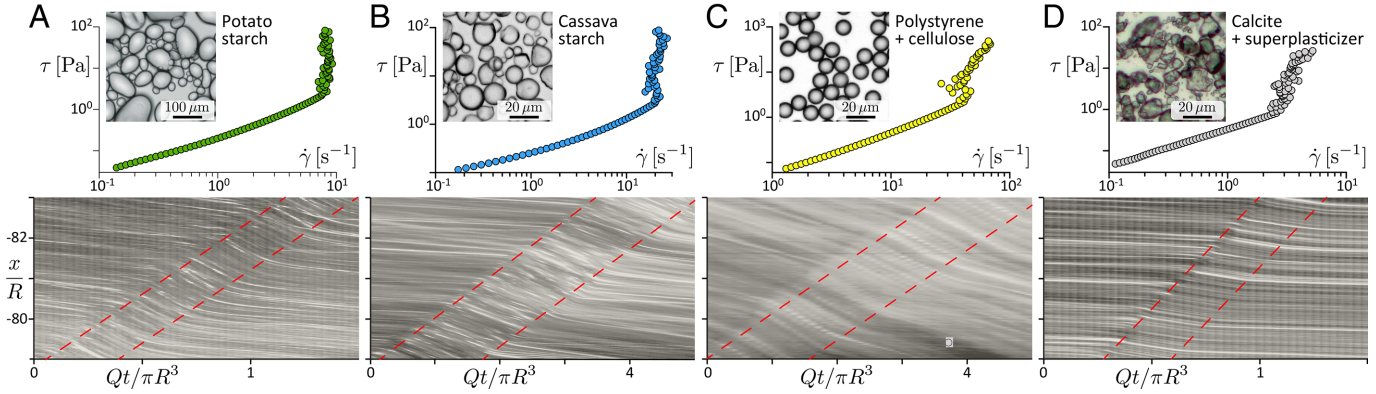

Fig. 6. Universality of the frictional soliton phenomenology. *Top*: rheograms for four different aqueous shear-thickening suspensions (70). *Bottom*: Spatiotemporal images of the near-wall flow at large forcing highlighting the same frictional-soliton phenomenology (the origin of t is arbitrary, here). (*A*) Potato-starch, (*B*) Cassava-starch, (*C*) Polystyrene spheres coated with cellulose, (*D*) Calcite grains ($CaCO_3$) + "superplasticizer" additive (polycarboxylate ether). $\phi = 0.42$, 0.448, 0.595, and 0.543, and $\langle \tau_w \rangle = 4.8$, 7.7, 138.5, and 41.5 Pa, respectively, see *M&M* and *SI Appendix*, SI.8.

accommodates the global overload with almost no change in the flow rate it sets.

Universality of the Frictional Soliton. All the observations and measurements discussed so far, concern suspensions of cornstarch. To probe the general relevance of the phenomenology reported above, we extend experiments to four other types of shear-thickening suspensions (Fig. 6) having different applicative context, particle shape, size polydispersity or composition: (*A* and *B*) potato and cassava starch grains, having a presumably similar biological polymeric-induced repulsion mechanism as cornstarch grains, but a more rounded shape and broader polydispersity, (*C*) highly monodisperse polystyrene spheres, coated with repulsive cellulosic polymers, and (*D*) calcite particles ($CaCO_3$)—a model fine granulometry component of high-performance concretes—which have a crystalline shape with sharp edges and are stabilized with an industrial admixture (polycarboxylate ether superplasticizer, kindly supplied by CHRYSO) aimed at improving flowability at high solid fractions. As shown in Fig. 6 (*Top*), dense aqueous suspensions of each of these particles present a similar discontinuously shear-thickening rheology, as cornstarch particles: a close to Newtonian behavior at low stress and a large and steep shear-thickening above a critical shear stress (see rheological characterization in *M&M* and *SI Appendix*, SI.8).

In all four cases, we observe a similar saturation of the pipe flow rate at large forcing, at a value approximately matching the expected saturation $Q_c \equiv (\pi R^3/4\eta_0)\tau_c$ inferred from rheological characterization ($0.8 \leq Q/Q_c \leq 4.6$, see *SI Appendix*, SI.8). The saturation is also found to result from the inception of a frictional soliton (Fig. 6, *Bottom*), whose length compares with the pipe diameter ($0.9 \leq l/2R \leq 1.5$), and velocity remains of the order of the mean flow velocity ($0.8 \leq c/U \leq 6.2$, the larger values being obtained with particles A and D). Last, near-wall velocimetry ($2 \leq U_w^{FS}/U_w \leq 8.3$) recovers that the cross-sectional velocity profile changes qualitatively from Poiseuille-like to plug-like flow within the soliton. These observations confirm that the phenomenology associated to the frictional soliton is not specific to cornstarch, but in fact relevant for a broad class of shear-thickening suspensions.

Discussion

The set of observations reported above draw a very unconventional picture of low-Reynolds pipe flows, in the particular case of shear-thickening suspensions. They reveal remarkable behaviors, both from a global perspective and in the structuration of the flow at the scale of the pipe radius R, which are controlled by the mean applied wall stress relative to the discontinuous shear-thickening onset $\tilde{\tau} \equiv \langle \tau_w \rangle / \tau_c(\phi) = -R\nabla P/2\tau_c(\phi)$. For highly concentrated suspensions ($\phi > \phi_{DST}$), a bifurcation of the flow is observed for $\tilde{\tau} \gtrsim 1$: a second flow phase, coined frictional soliton, nucleates and coexists with the steady, laminar, Poiseuille-like flow obtained at low applied stress. The frictional soliton is a longitudinally localized, upstream propagative, shape-preserving flow structure, which spans the pipe cross-section. It is, above all, a superdissipative structure, concentrating most of the dissipation over a flow length of order R. Its steep (local) resistance law, summarized by Eq. **2** and valid at the pipe radius scale, actually determines the singularly steep resistance law at the whole pipe scale (Eqs. **3** and **4**), i.e., a Poiseuille law, for low applied stress, continued by a saturation of the flow rate, at higher stress, at a value $\approx Q_c \equiv \pi R^3 \tau_c(\phi)/4\eta_0$ set by $\tau_c(\phi)$ and the low-stress (frictionless) viscosity η_0.

Various aspects of this remarkable phenomenology require comments. First, it does not depend on flow inertia. Regarding the inception of the frictional soliton, the same onset stress ($\tilde{\tau} = 1$) is observed for a broad range of Reynolds numbers ($Re = \rho Q/\pi\eta_0 R \sim 10^{-2} - 10$), as R is varied. Regarding the self-sustained propagation, the local effective viscosity in the soliton $\sim \pi R^3 \tau_w^{FS}/4Q_c$, is larger than the laminar phase viscosity η_0 by a factor $\sim \tau_w^{FS}/\tau_c(\phi) \sim L/\ell$, see Eq. **2**. Hence, the relevant local Reynolds number $\sim (\ell/L)Re \sim 10^{-4} - 10^{-1}$ is much below 1, which confirms the subdominant role of inertia in the soliton dynamics.

Second, the emergence of a localized propagative flow phase (the frictional soliton) coexisting with a laminar phase, is reminiscent of other solitary waves or intermittent flow structures so far identified in pipe flows at high forcings, such as turbulent puffs and slugs in the inertial transition regime (4, 7, 8, 10), density/concentration waves in compressible or incompressible two-phase media (50–53), or bulging waves in elastically or viscously compliant pipes (54–56). However, the frictional soliton is distinct in nature from these previously reported examples. For instance, inertial puffs are memoryless structures, which stochastically nucleate, decay, and coexist (6, 7), without affecting drastically the global resistance or flow rate, because the local resistance law of the puff/slug phases is not steep enough (9) (*Inset* of Fig. 5*B*). In contrast, frictional solitons are characterized by their deterministic uniqueness—in the range of parameter investigated, one and only one soliton actually

emerges and propagates above $\tau_c(\phi)$—and their singularly steep resistance law, Eq. **2**. This law and the low bulk compressibility of the suspension (liquid+grains) imply that the nucleation of a frictional soliton affects the resistance of the whole pipe flow within milliseconds ($\sim L/c_{\text{sound}}$, with $c_{\text{sound}} \sim 1$ km/s the sound speed), and acts as a particularly efficient flow limiter, accommodating large variations in the total applied load with minimal change in the flow rate. They also allow the uniqueness of the soliton, since the resulting saturation of the flow rate at Q_c maintains the coexisting flow phase in a frictionless, hence laminar, state. Note, however, that a different phenomenology might emerge for sufficiently slender pipes or high applied stresses, since the stress in the soliton $\sim(L/R)\langle\tau_w\rangle$ could deform the particles or trigger cavitation.

The phenomenology of the frictional soliton also differs, qualitatively, from the mechanisms proposed so far for other unsteady shear-thickening flows. At high stress, these flows feature large stress and velocity fluctuations (29, 36, 57), but these are small scale, intermittent or chaotic structures. Coherent propagative structures, such as jamming fronts, have also been reported in shear flows, but these are intrinsically inertial fronts which propagate transversely to the flow with a large velocity depending strongly on volume fraction (35, 41–44). Stress and concentration bands traveling either parallel (36, 37) or perpendicular (30, 31) to the flow direction have also been observed and modeled, but none of them have been shown to develop upstream propagative solitary waves. Specific noninertial surface waves have also been reported and modeled (33, 34, 58), but the mechanism, involving the free surface, does not apply to wall-bounded flows. Last, upstream propagative density waves have been observed for flows in capillaries (52, 53), but these are not mutually exclusive and develop only in capillaries with diameter of a few particle sizes. Perhaps the most similar phenomenology to the frictional soliton has been observed in a plate-plate Couette flow, with jammed structures propagating both upstream and downstream at speeds close to the forcing velocity (36, 38, 39, 59). No mechanism has been proposed so far, but pore-scale measurements of the relative velocity between the particles and the suspending liquid suggest that these structures involve strongly localized dilation of the suspension (39), which is also consistent with the bubble expansion observed in the frictional soliton (Fig. 3*D*).

These latter observations suggest that particle dilation and the coupling with the suspending liquid are essential ingredients to explain the propagation and the high dissipation in the frictional soliton. We propose the following minimal mechanism based on the observed length of the soliton and its formation at the pipe outlet. As the soliton passes a slab of suspension, the shear stress close to the wall builds up above the onset jamming stress, of order $\tau_c(\phi)$, beyond which the suspension must dilate to flow. This Reynolds-like dilation of the particle phase (60, red arrows in Fig. 7) lowers the particle volume fraction in a thin layer of suspension close to the wall and eventually the drag of the suspension slab, until the local shear stress decreases below the critical stress $\tau_c(\phi)$ and the suspension slab returns to a laminar flow. The dilation occurs over a typical strain $\gamma_0 \sim \mathcal{O}(1)$ independent of ϕ (61, 62), i.e., over a typical time scale $t_D \sim \gamma_0/\dot{\gamma} \sim \gamma_0 R/U$, since the near-wall shear rate in the soliton is of order U/R (*SI Appendix*, SI.4). Given the formation of the soliton at the pipe outlet and its length $\ell \sim 2R$, this explains why the soliton propagates upstream and with a velocity $c \sim \ell/t_D \sim 2U/\gamma_0$ of the order of the mean flow velocity.

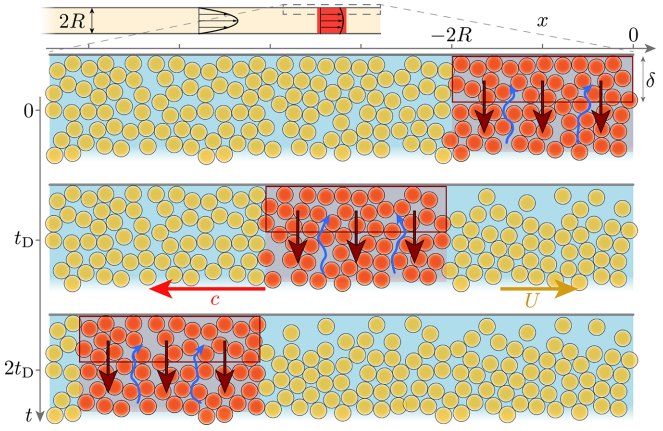

Fig. 7. Minimal mechanism for the frictional-soliton propagation. As the soliton passes a slab of suspension: (*i*) the shear stress builds up above τ_c and the suspension jams over a length scale set by the pipe diameter $2R$, (*ii*) the steady flow rate forces the jammed suspension, which dilates at the wall, over a layer of thickness δ and a time scale $t_D \sim \gamma_0/\dot{\gamma} \sim \gamma_0 R/U$, (*iii*) because of the particle-depleted layer, the local shear stress relaxes below τ_c, which builds up the shear stress immediately upstream. The soliton thus propagates upstream at a velocity $c \sim \ell/t_D \sim 2U/\gamma_0$, of the order of the mean flow velocity U.

This mechanism also explains how the stress τ_w in the soliton accommodates the possibly large excess load imposed at the pipe scale. The dilation involves a flow of the suspending liquid across the pores (blue arrows), which results in a large negative pore pressure, i.e., a large positive particle stress, whose magnitude is given by a Darcy–Reynolds scaling $\tau_w \sim (\eta_l/\kappa)(\Delta\phi/\gamma_0)\delta^2 U/R$ (62, 63), with η_l the suspending liquid viscosity, $\kappa \sim 10^{-3}d^2$ the permeability of the particle phase, d the particle diameter, $\Delta\phi \sim 10^{-2}$ the distance to jamming, and δ the thickness of the dilation layer (Fig. 7). A dilation layer of the order of the pipe radius ($\delta \sim R \sim 300d$) is enough to build a wall stress $\tau_w \sim 10(\delta/d)^2\eta_l U/R \sim 10^4\eta_0 U/R$, orders of magnitude larger than the laminar phase shear stress $\sim\eta_0 U/R$, providing room to accommodate a high external load. This minimal dilation mechanism captures the main features of the soliton phenomenology. It also agrees qualitatively with the observation of a slight, but systematic, increase in the flow rate as the second generation of frictional soliton propagates in the pipe (the particle-depleted layer is expected to shift the critical flow rate toward larger values). However, the nucleation mechanism and the selection of the soliton length remain to be elucidated. Further modeling and additional experimental inputs, in particular about the evolution of the concentration and velocity profiles, are also required to understand how the flow sets the near-wall shear rate and the thickness of the dilation layer δ.

Last, the singular steepness of the global resistance law and the frictional soliton are robustly observed with various particle systems (different natural starch grains, polymer-grafted plastic beads, calcite powder stabilized with a superplasticizer), which supports their universality for pipe flows of shear-thickening suspensions and their potential relevance to improve pumping in industrial applications. For instance, in civil engineering, superplasticizers, which are commonly added with fine materials (fly ash, silica fume) to enhance concrete flowability, make the concrete shear-thickening (64–68). This concrete is often pumped through long ($L/R \gtrsim 10^4$) and wide pipes ($R/d \gtrsim 10^3$) at high mean wall stress (reaching $10^2 - 10^3\,\tau_c$), and further

study will have to determine whether the frictional-soliton phenomenology extends to such large forcings.

Materials and Methods

Setup. The pipe is a 2 m-long, transparent, smooth, PMMA tube, with inner radius $R \simeq 3$, 5.15 or 17 mm. The scale has a precision of 0.01 g and a response time of 0.2 s. The four pressure gauges S_1 to S_4 are located 0.1, 0.3, 0.5, and 0.7 m from the pipe outlet, respectively. Different gauges (with ranges from 3.7 to 100 kPa, precisions from 0.1 to 1 kPa, and a response time of 1 ms) are used for the different forcings. The near-wall flow is imaged between S_2 and S_3, under laser diode illumination (2 W, 532 nm), with a camera (JAI, 4,096 × 3,072 pixels) at a spatial resolution of 10 μm/pixel and acquisition rate up to 300 Hz. The fluorescent tracing particles are 20 μm, spherical, PMMA particles doped with rhodamine 6G (69). To prevent image distortion by the curved pipe wall, the pipe is surrounded with a rectangular chamber (40 × 25 × 25 mm) filled with a liquid (Triton X-100) of same refractive index as the pipe wall.

Materials. The shear-thickening suspensions consist mainly of commercial cornstarch grains (Maisita®, $\rho_p = 1{,}550\ \mathrm{kg/m^3}$) mixed with microfiltered water ($\rho_w = 997\ \mathrm{kg/m^3}$). The particle volume fraction ϕ of the suspensions is computed from the weight and density of the dry particles and liquid. The suspension density is given by $\rho = \rho_p\phi + \rho_w(1-\phi)$. Prior to use, the starch is systematically desiccated with the same protocol (a few days at 60 °C in an oven) to avoid shifts in dry density due to air moisture variations. The potato starch grains, cassava starch grains and polystyrene spheres are commercial (respectively, Roquette® with $\rho_p = 1{,}500\ \mathrm{kg/m^3}$, New Land® with $\rho_p = 1{,}550\ \mathrm{kg/m^3}$, and TS by Dynoseeds®, with diameter $10.1 \pm 0.3\ \mu\mathrm{m}$ and $\rho_p = 1{,}050\ \mathrm{kg/m^3}$). The calcite particles (Omya®, $\rho_p = 2{,}700\ \mathrm{kg/m^3}$) are sieved with a 30 μm mesh. The industrial superplasticizer (polycarboxylate ether, kindly supplied by Chryso®) is added to the suspension at 3 wt‰.

Rheological Characterization. The rheograms in Figs. 1*B* and 6 *A–C* are obtained using rough, coaxial cylinders (height of 38.7 mm, inner and outer radii of 13.55 and 15.63 mm, respectively). The flow curve are obtained as the average over three logarithmically increasing torque ramps, after a preshear. To limit migration effects above the shear-thickening onset, the suspension is floated on a heavier, nonmiscible and low-viscosity oil (perfluorotributylamine, Fluorinert FC-43). Because calcite (much denser than water and Fluorinert) settles rapidly, the Newtonian-effective rheogram in Fig. 6*D* is obtained from the torque on a homemade helix (diameter of 35 mm, with two levels of tilted blades) rotating at a low Reynolds number ($\lesssim 0.3$) inside a rough cup (diameter of 39 mm), which is calibrated against a potato starch shear-thickening suspension.

Experimental Procedure and Additional Tests. Procedure (variations, in parenthesis, have been tested without change on the phenomenology): i) The pipe is inclined at $\theta = 7°$, below the shear-thickening threshold, and slowly filled with the freshly mixed suspension from one end (or the other), while it is continuously rotated to prevent sedimentation. ii) The pipe outlet is obturated and tilted to the desired flow inclination θ, with the outlet located $\sim 2R$ above (or beneath) the surface of a water pool to reduce (cancel) stress in the extruded suspension jet. iii) The plug is removed to start the flow. Additional tests: i) The frictional soliton can be incepted after flow start, either by increasing the inclination above the critical only after flow initiated, or by removing a rod placed across the pipe to obstruct the flow. ii) Use of a roughened pipe (obtained by gluing two sand-blasted half-pipes) yields the same saturation flow rate ($Q/Q_c \approx 0.5$ to 1), soliton length ($\ell/2R \approx 0.3$ to 1) and soliton velocity ($c/U \approx 1.6$ to 2.5).

Data, Materials, and Software Availability. Experimental data have been deposited in Zenodo (http://doi.org/10.5281/zenodo.10287701) (70).

ACKNOWLEDGMENTS. This work was funded by ANR ScienceFriction (ANR-18-CE30-0024) and ANR SuJets (ANR-21-CE30-0015-01).

1. J. Poiseuille, Recherches expérimentales sur le mouvement des liquides dans les tubes de très petits diamètres. *C. R. Acad. Sci.* **11**, 961–967 (1840).
2. G. Hagen, Über die bewgung des wassers in engen cylindrischen röhren. *Ann. Phys. (Berl.)* **46**, 423–442 (1839).
3. S. Sutera, R. Skalak, The history of Poiseuille's law. *Annu. Rev. Fluid. Mech.* **25**, 1–19 (1993).
4. O. Reynolds, An experimental investigation of the circumstances which determine whether the motion of water in parallel channels shall be direct or sinuous, and of the law of resistance in parallel channels. *Phil. Trans. R. Soc.* **174**, 935–982 (1883).
5. I. Wygnanski, F. Champagne, On transition in a pipe. Part 1. The origin of puffs and slugs and the flow in a turbulent slug. *J. Fluid Mech.* **59**, 281–335 (1973).
6. A. Darbyshire, T. Mullin, Transition to turbulence in constant-mass-flux pipe flow. *J. Fluid Mech.* **289**, 83–114 (1995).
7. B. Eckhardt, T. Schneider, B. Hof, J. Westerweel, Turbulence transition in pipe flow. *Annu. Rev. Fluid. Mech.* **39**, 447–468 (2007).
8. T. Mullin, Experimental studies of transition to turbulence in a pipe. *Annu. Rev. Fluid. Mech.* **43**, 1–24 (2011).
9. R. Cerbus, C.-C. Liu, G. Gioia, P. Chakraborty, Laws of resistance in transitional pipe flows. *Phys. Rev. Lett.* **116**, 054502–054505 (2018).
10. M. Avila, D. Barkley, B. Hof, Transition to turbulence in pipe flow. *Annu. Rev. Fluid. Mech.* **55**, 575–602 (2023).
11. A. Metzner, J. Reed, Flow of non-Newtonian fluids-correlation of the laminar, transition, and turbulent-flow regions. *AIChE J.* **1**, 434–440 (1955).
12. R. Griskey, R. Green, Flow of dilatant (shear-thickening) fluids. *AIChE J.* **17**, 725–728 (1971).
13. D. Leighton, A. Acrivos, The shear-induced migration of particles in concentrated suspensions. *J. Fluid Mech.* **181**, 415–439 (1987).
14. R. Hampton, A. Mammoli, A. Graham, N. Tetlow, Migration of particles undergoing pressure-driven flow in a circular conduit. *J. Rheol.* **41**, 621–640 (1997).
15. G. Gadd, Turbulence damping and drag reduction produced by certain additives in water. *Nature* **206**, 463–467 (1965).
16. Y. Cho, J. Harnett, Non-Newtonian fluids in circular pipe flow. *Adv. Heat Transf.* **15**, 59–141 (1982).
17. F. Pinho, J. Whitelaw, Flow of non-Newtonian fluids in a pipe. *J. Non-Newton. Fluid Mech.* **34**, 129–144 (1990).
18. J.-P. Matas, J. Morris, E. Guazzelli, Transition to turbulence in particulate pipe flow. *Phys. Rev. Lett.* **90**, 014501 (2003).
19. J. Peixinho, C. Nouar, C. Desaubry, B. Théron, Laminar transitional and turbulent flow of yield stress fluid in a pipe. *J. Non-Newton. Fluid Mech.* **128**, 172–184 (2005).
20. G. Bossis, Y. Grasselli, O. Volkova, Capillary flow of a suspension in the presence of discontinuous shear thickening. *Rheol. Acta* **61**, 1–12 (2022).
21. D. Feys, R. Verhoeven, G. De Schutter, Fresh self compacting concrete, a shear thickening material. *Cem. Concr. Res.* **38**, 920–929 (2008).
22. E. Blanco *et al.*, Conching chocolate is a prototypical transition from frictionally jammed solid to flowable suspension with maximal solid content. *Proc. Natl. Acad. Sci. U.S.A.* **116**, 10303–10308 (2019).
23. J. Higgins, D. Eddington, S. Bhatia, L. Mahadevan, Sickle cell vasoocclusion and rescue in a microfluidic device. *Proc. Natl. Acad. Sci. U.S.A.* **104**, 20496–20500 (2007).
24. J. Smith, Shear-thickening dilatancy in crystal-rich flows. *J. Volcanol. Geotherm. Res.* **79**, 1–8 (1997).
25. J. Smith, Textural evidence for dilatant (shear thickening) rheology of magma at high crystal concentrations. *J. Volcanol. Geotherm. Res.* **99**, 1–7 (2000).
26. R. Mari, R. Seto, J. Morris, M. Denn, Shear thickening, frictionless and frictional rheologies in non-Brownian suspensions. *J. Rheol.* **58**, 1693–1724 (2014).
27. M. Wyart, M. Cates, Discontinuous shear thickening without inertia in dense non-Brownian suspensions. *Phys. Rev. Lett.* **112**, 098302 (2014).
28. C. Clavaud, A. Bérut, B. Metzger, Y. Forterre, Revealing the frictional transition in shear-thickening suspensions. *Proc. Natl. Acad. Sci. U.S.A.* **114**, 5147–5152 (2017).
29. M. Hermes *et al.*, Unsteady flow and particle migration in dense, non-Brownian suspensions. *J. Rheol.* **60**, 905–916 (2016).
30. R. Chacko, R. Mari, M. Cates, S. Fielding, Dynamic vorticity banding in discontinuously shear thickening suspensions. *Phys. Rev. Lett.* **121**, 108003 (2018).
31. B. Saint-Michel, T. Gibaud, S. Manneville, Uncovering instabilities in the spatiotemporal dynamics of a shear-thickening cornstarch suspension. *Phys. Rev. X* **8**, 031006 (2018).
32. J. Richards, J. Royer, B. Liebchen, B. Guy, W. Poon, Competing timescales lead to oscillations in shear-thickening suspensions. *Phys. Rev. Lett.* **123**, 038004 (2019).
33. B. Darbois Texier, H. Lhuissier, Y. Forterre, B. Metzger, Surface-wave instability without inertia in shear-thickening suspensions. *Commun. Phys.* **232**, 232 (2020).
34. B. Darbois Texier, H. Lhuissier, B. Metzger, Y. Forterre, Shear-thickening suspensions down inclines: From Kapitza to Oobleck waves. *J. Fluid Mech.* **959**, A27 (2023).
35. I. Peters, S. Majumdar, H. Jaeger, Direct observations of dynamic shear jamming in dense suspensions. *Nature* **532**, 214–217 (2016).
36. V. Rathee, D. Blair, J. Urbach, Localized stress fluctuations drive shear thickening in dense suspensions. *Proc. Natl. Acad. Sci. U.S.A.* **114**, 8740–8745 (2017).
37. G. Ovarlez *et al.*, Density waves in shear-thickening suspensions. *Sci. Adv.* **6**, eaay5589 (2020).
38. A. Gauthier, M. Pruvost, O. Gamache, A. Colin, A new pressure sensor array for normal stress measurement in complex fluids. *J. Rheol.* **65**, 583–594 (2021).
39. V. Rathee, J. Miller, D. Blair, J. Urbach, Structure of propagating high-stress fronts in a shear-thickening suspension. *Proc. Nat. Acad. Sci. U.S.A.* **119**, e2203795119 (2022).
40. H. Freundlich, H. Röder, Dilatancy and its relation to thixotropy. *Trans. Faraday Soc.* **34**, 308–316 (1938).
41. F. Rocha, Y. Forterre, B. Metzger, H. Lhuissier, Drag of a shear-thickening suspension on a rotating cylinder. *J. Fluid Mech.* **970**, A35–19 (2023).

42. S. Waitukaitis, H. Jaeger, Impact-activated solidification of dense suspensions via dynamic jamming fronts. *Nature* **487**, 205–209 (2012).
43. I. Han, E. Peters, H. Jaeger, High-speed ultrasound imaging in dense suspensions reveals impact-activated solidification due to dynamic shear jamming. *Nat. Commun.* **7**, 12243 (2016).
44. E. Han, M. Wyart, I. Peters, H. Jaeger, Shear fronts in shear-thickening suspensions. *Phys. Rev. Fluids* **3**, 073301 (2018).
45. A. Deboeuf, G. Gauthier, J. Martin, Y. Yurkovetsky, J. Morris, Particle pressure in a sheared suspension: A bridge from osmosis to granular dilatancy. *Phys. Rev. Lett.* **102**, 108301 (2009).
46. S. Kulkarni, B. Metzger, J. Morris, Particle-pressure-induced self-filtration in concentrated suspensions. *Phys. Rev. E* **82**, 010402 (2010).
47. T. Dbouk, L. Lobry, E. Lemaire, Normal stresses in concentrated non-Brownian suspensions. *J. Fluid Mech.* **715**, 239–272 (2013).
48. R. Larsen, J.-W. Kim, C. Zukoski, D. Weitz, Fluctuations in flow produced by competition between apparent wall slip and dilatancy. *Rheol. Acta* **53**, 333–347 (2014).
49. B. Etcheverry, Y. Forterre, B. Metzger, Capillary-stress controlled rheometer reveals the dual rheology of shear-thickening suspensions. *Phys. Rev. X* **13**, 011024 (2023).
50. T. Raafat, J.-P. Hulin, H. Herrmann, Density waves in dry granular media falling through a vertical pipe. *Phys. Rev. E* **53**, 4345–4350 (1996).
51. A. Nakahara, T. Isoda, $1/f^{\alpha}$ density fluctuation at the slugging transition point of granular flows through a pipe. *Phys. Rev. E* **55**, 4264–4273 (1997).
52. L. Isa, R. Besseling, A. Morozov, W. Poon, Velocity oscillations in microfluidic flows of concentrated colloidal suspensions. *Phys. Rev. Lett.* **102**, 058302 (2009).
53. P. Kanehl, H. Stark, Self-organized velocity pulses of dense colloidal suspensions in microchannel flow. *Phys. Rev. Lett.* **119**, 018002–018006 (2017).
54. S. Aktershev, A. Fedorov, V. Fomin, Propagation of a soliton along a fluid-filled pipe. *J. Appl. Mech. Tech. Phys.* **27**, 370–375 (1986).
55. D. Scott, D. Stevenson, J. Whitehead, Observation of solitary waves in a viscously deformable pipe. *Nature* **319**, 759–761 (1986).
56. M. Maiden, N. Lowman, D. Anderson, M. Schubert, M. Hoefer, Observation of dispersive shock waves, solitons, and their interactions in viscous fluid conduits. *Phys. Rev. Lett.* **116**, 174501–174505 (2016).
57. O. Sedes, A. Singh, J. F. Morris, Fluctuations at the onset of discontinuous shear thickening in a suspension. *J. Rheol.* **64**, 309–319 (2020).
58. N. Balmforth, J. Bush, R. Craster, Roll waves on flowing cornstarch suspensions. *Phys. Lett. A* **338**, 479–484 (2005).
59. R. Maharjan, E. O'Reilly, T. Postiglione, N. Klimenko, E. Brown, Relation between dilation and stress fluctuations in discontinuous shear thickening suspensions. *Phys. Rev. E* **103**, 012603 (2021).
60. O. Reynolds, LVII. On the dilatancy of media composed of rigid particles in contact. With experimental illustrations. *Lond. Edinb. Dubl. Phil. Mag.* **20**, 469–481 (1885).
61. M. Pailha, O. Pouliquen, A two-phase flow description of the initiation of underwater granular avalanches. *J. Fluid Mech.* **633**, 115–135 (2009).
62. S. Athani, B. Metzger, Y. Forterre, R. Mari, Transient flows and migration in granular suspensions: Key role of Reynolds-like dilatancy. *J. Fluid Mech.* **949**, A9 (2022).
63. J. Jerome, N. Vandenberghe, Y. Forterre, Unifying impacts in granular matter from quicksand to cornstarch. *Phys. Rev. Lett.* **117**, 098003 (2016).
64. M. Cyr, C. Legrand, M. Mouret, Study of the shear thickening effect of superplasticizers on the rheological behaviour of cement pastes containing or not mineral additives. *Cem. Concr. Res.* **30**, 1477–1483 (2000).
65. D. Feys, R. Verhoeven, G. De Schutter, Why is fresh self-compacting concrete shear thickening? *Cem. Concr. Res.* **39**, 510–523 (2009).
66. A. Yahia, Shear-thickening behavior of high-performance cement grouts - Influencing mix-design parameters. *Cem. Concr. Res.* **41**, 230–235 (2011).
67. D. Feys, R. Verhoeven, G. De Schutter, Pumping of fresh concrete: Insights and challenges. *RILEM Tech. Lett.* **1**, 76–80 (2016).
68. J. Richards, R. O'Neil, W. Poon, Turning a yield-stress calcite suspension into a shear-thickening one by tuning inter-particle friction. *Rheol. Acta* **60**, 97–106 (2021).
69. B. Metzger, J. Butler, Clouds of particles in a periodic shear flow. *Phys. Fluids* **24**, 021703 (2012).
70. A. Bougouin, B. Metzger, Y. Forterre, P. Boustingorry, H. Lhuissier, Data of A frictional soliton controls the resistance law of shear-thickening suspensions in pipes. Zenodo. http://doi.org/10.5281/zenodo.10287700. Deposited 2 April 2024.

Supplementary Information for 'A frictional soliton controls the resistance law of shear-thickening suspensions in pipes'

Alexis Bougouin[a], Bloen Metzger[a], Yoel Forterre[a], Pascal Boustingorry[b], and Henri Lhuissier[a,1]

[a]Aix Marseille Univ, CNRS, IUSTI, Marseille, France; [b]CHRYSO, 7 rue de l'Europe, F-45300 Sermaises, France

Contents of this file

SI.1. Description of the experimental movies

The movies show the near-wall flow for a cornstarch suspension. They correspond to the spatio-temporal diagram provided in Fig. 3 of the main body of the paper.

Movies 1 & **2** show the flow in the low-forcing regime and in the high-forcing regime, respectively ($\phi = 0.405$). **Movie 1:** low-forcing regime (Fig 3A, $\theta = 4.9°$, i.e., $\langle\tau_w\rangle = 2.6$ Pa and $\langle\tau_w\rangle/\tau_c \approx 0.7$, $Q \approx 1.36$ ml/s). **Movie 2:** high-forcing regime (Fig 3B, $\theta = 22.0°$, i.e., $\langle\tau_w\rangle = 11.6$ Pa and $\langle\tau_w\rangle/\tau_c \approx 2.9$, $Q \approx 1.24$ ml/s).

Movie 3 shows the growth of small air bubbles, fortuitously transported by the suspension, as the frictional soliton passes (Fig 3D, $\phi = 0.39$, $\theta = 42.0°$, i.e., $\langle\tau_w\rangle = 20.5$ Pa and $\langle\tau_w\rangle/\tau_c \approx 3.7$).

For all three movies, the pipe radius is $R = 5.15$ mm and spatial resolution is 10 µm/pixel. Lengths are indicated by scale bars. Movie 1 and 2 are displayed in real time. Movie 3 is slowed-down by a factor 10. More information about optical measurements are given in *M&M* in the main body of the paper.

SI.2. Preliminary experiments with a reservoir at the pipe inlet

Preliminary experiments have been conducted with a horizontal, smooth PMMA tube (length $L = 0.5$ m, inner radius $R = 1.6$ mm) connected to a large feed reservoir (Fig. SI.1). The flow is driven by setting a pressure difference, $\rho gH + P_{\text{air}}$, between the pipe inlet and outlet, with the help of a constant air overpressure P_{air}. In the case where inertial effects are small and the localized entrance dissipation is small relative to the regular dissipation along the pipe, this corresponds to a mean applied pressure gradient along the pipe $\langle -\nabla P\rangle \equiv (\rho gH + P_{\text{air}})/L$. The pressure in the pipe is measured with sensors located 0.1, 0.2, 0.3 and 0.4 m from the pipe outlet.

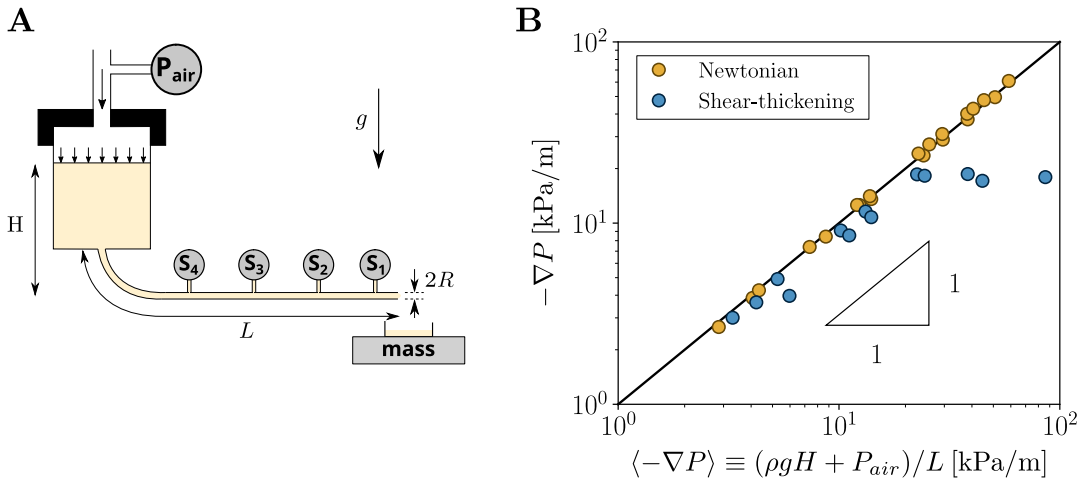

Fig. SI.1. (A) Sketch of the setup of the preliminary experiments with a feed reservoir. (B) Local pressure gradient in the pipe versus mean applied pressure gradient for a Newtonian liquid (see text) and a shear thickening suspension (10 µm polystyrene spheres in water, $\phi = 0.59 > \phi_{\text{DST}} \approx 0.575$).

For experiments with a Newtonian liquid (40%w aqueous solution of PEPG (3.9 kg/mol poly(ethylene glycol-ran-propylene glycol)-monobutyl-ether by Sigma-Aldrich) with viscosity $\eta \approx 0.4$ Pa s and density $\rho \approx 1066$ kg/m^3) at low Reynolds number ($\lesssim 0.2$), the local pressure gradient $-\nabla P$, as measured in the pipe, is found to be very close to the mean pressure gradient $\langle -\nabla P \rangle \equiv (\rho g H + P_{\rm air})/L$. This agrees with the expectation, for the present case of a long pipe ($L/R \sim 300 \gg 1$), that localized entrance losses ($\sim \eta U/R$, with U the mean flow velocity) are small relative to the regular losses along the pipe ($\sim \eta U L/R^2$).

By contrast, experiments with shear-thickening suspensions reveal a mismatch between the local pressure gradient $-\nabla P$ and the mean imposed gradient $\langle -\nabla P \rangle$, at high applied pressure. For $\langle -\nabla P \rangle \gtrsim 20$ kPa/m, the gradient in the pipe actually saturates at a value $-\nabla P \sim 20$ kPa/m (blue disks in Fig. SI.1). This saturation of $-\nabla P$ is associated with a saturation of the flow rate (data not shown), which agrees with observations by (1) on a similar configuration. Importantly, our measurements show that for $\langle -\nabla P \rangle \gtrsim 20$ kPa/m the gradient is identical over each measurement portion of the pipe (S_1S_2, S_2S_3 and S_3S_4), and fixed in time. This indicates that the converging flow at the entrance of the pipe causes a large localized dissipation (presumably similar with that reported for the flow of a shear-thickening suspension through an orifice (2)), which is *fixed* at the pipe inlet and affects the whole pipe flow.

To prevent these large entrance effects and address the intrinsic flow in a pipe, we have used the drainage setup presented in the main body of the paper.

SI.3. Laminar base-state flow expected for a Wyart-Cates rheology

Model. For a steady laminar flow, driven by a uniform gravitational component $g \sin\theta$, the longitudinal velocity $u(r)$ at radial coordinate r is

$$u(r) = \int_r^R \dot\gamma(r)\,\mathrm{d}r = \int_r^R \frac{\tau(r)}{\eta(r)}\,\mathrm{d}r\,, \qquad \text{[SI.1]}$$

with $\dot\gamma(r) = -\partial u/\partial r = \tau(r)/\eta$ the local shear rate, $\tau(r) = \rho g r \sin\theta/2$ the local shear stress, ρ and η the density and effective viscosity of the flowing material, respectively, and R the pipe radius, at which a no-slip condition ($u(R) = 0$) is assumed (Fig. SI.2A). Making use of $r = 2\tau/\rho g \sin\theta$, Eq. [SI.1] can be recasted into

$$u(\tau) = \frac{2}{\rho g \sin\theta} \int_\tau^{\tau_w} \frac{\tau}{\eta(\tau)}\,\mathrm{d}\tau\,, \qquad \text{[SI.2]}$$

with $\tau_w = \langle \tau_w \rangle = \tau(r = R)$ the uniform wall stress.

The model rheological shear-thickening laws proposed by Wyart-Cates (3), assumes that the effective viscosity of the suspension depends on the magnitude of the shear stress relative to the inter-particle repulsive stress scale τ^*, according to $\eta = \eta_S(\phi_J - \phi)^{-2}$, with η_S a prefactor of order the suspending liquid viscosity, $\phi_J = (1-f)\phi_0 + f\phi_1$ the jamming volume fraction for a given stress τ, ϕ_0 and ϕ_1 the frictionless and frictional jamming volume fractions, respectively, and $f = \exp(-\tau^*/\tau)$ the stress-dependent fraction of frictional contacts between the particles in the suspension, i.e.,

$$\eta(\tau) = \eta_S\,[\phi_0 - (\phi_0 - \phi_1)\mathrm{e}^{-\tau^*/\tau} - \phi]^{-2}\,, \qquad \text{[SI.3]}$$

of which the four physical parameters (η_S, ϕ_0, ϕ_1, τ^*) must be determined from rheological measurements.

Combining Eqs. [SI.2-SI.3], the velocity profile and the flow rate, are obtained, respectively, as

$$u(\tau) = \frac{2}{\eta_S \rho g \sin\theta} \int_\tau^{\tau_w} \frac{\tau}{[\phi_0 - (\phi_0 - \phi_1)\mathrm{e}^{-\tau^*/\tau} - \phi]^{-2}}\,\mathrm{d}\tau\,, \qquad Q(\tau) = \frac{2\pi R^2}{{\tau_w}^2} \int_0^{\tau_w} u(\tau)\tau\,\mathrm{d}\tau\,. \qquad \text{[SI.4]}$$

Rheological data fitting procedure. The parameters η_s, ϕ_0, ϕ_1 and τ^* for the cornstarch suspensions are obtained by fitting Eq. [SI.3] to the rheological measurements (see *M&M* in the main body of the paper for information about the measurements). First, the low stress (circles) and high stress (squares) viscosity branches, are jointly fitted with $\eta = \eta_S(\phi_0 - \phi)^{-2}$ and $\eta = \eta_S(\phi_1 - \phi)^{-2}$, respectively, to determine $\eta_S = 0.28$ mPa.s, $\phi_0 = 0.445$ and $\phi_1 = 0.385$ (Fig. SI.2B-left). This also sets the minimal volume fraction for discontinuous shear thickening $\phi_{\rm DST} = \phi_0 - 2\mathrm{e}^{-1/2}(\phi_0 - \phi_1) \approx 0.37$. Second, the repulsive stress scale τ^* is obtained by fitting the whole data set, which gives $\tau^* = 8.0$ Pa (Fig. SI.2B-right). Despite their simplicity, the Wyart-Cates rheological laws are found to fit fairly well the global trends of the rheological measurements (except for the negatively-sloped region, where measurements are not expected to reflect the rheological response of the suspension because of flow instabilities leading to large deviations from a laminar rheometric flow (4–6)). In particular, they fit fairly well the evolution of the non-frictional viscosity, $\eta_0(\phi) \equiv \eta_S(\phi_0 - \phi)^{-2}$, and of the critical shear stress, $\tau_c(\phi)$, with the particle volume fraction ϕ.

Laminar base-state velocity profile and flow rate. Fig. SI.2C, presents the laminar base-state velocity profile and flow rate (Eq. [SI.4]) using the rheological parameters fitted on the rheograms of cornstarch suspensions (Fig. SI.2B). The velocity profile, normalized by the maximal velocity $u_{\rm max} = u(r = 0)$, is plotted for a fixed volume fraction $\phi = 0.41 > \phi_{\rm DST}$ and relative wall stresses τ_w/τ^* ranging from 0.1 to 10. The normalized flow rate, $\eta_S Q/R^3\tau^*$, is plotted as a function of τ_w/τ^* for particle volume fractions between 0.30 and 0.44. For low wall stresses ($\tau_w \ll \tau_c \approx 0.4\tau^*$), the velocity profile is close to parabolic and the flow rate follows Hagen-Poiseuille law $Q = \frac{\pi R^3}{4\eta_0}\langle\tau_w\rangle \propto \langle\tau_w\rangle$, with $\eta_0 = \eta_S(\phi_0 - \phi)^{-2}$ the frictionless viscosity. As stress is increased much above τ_c, an increasingly large portion of the suspension next to the wall is expected to jam, and the base-state flow rate decreases, asymptotically, as $Q \sim (R^3\tau_c/\eta_0) \times (\tau_c/\tau_w)^3 \propto \tau_w^{-3}$.

[1] To whom correspondence should be addressed: henri.lhuissier@univ-amu.fr

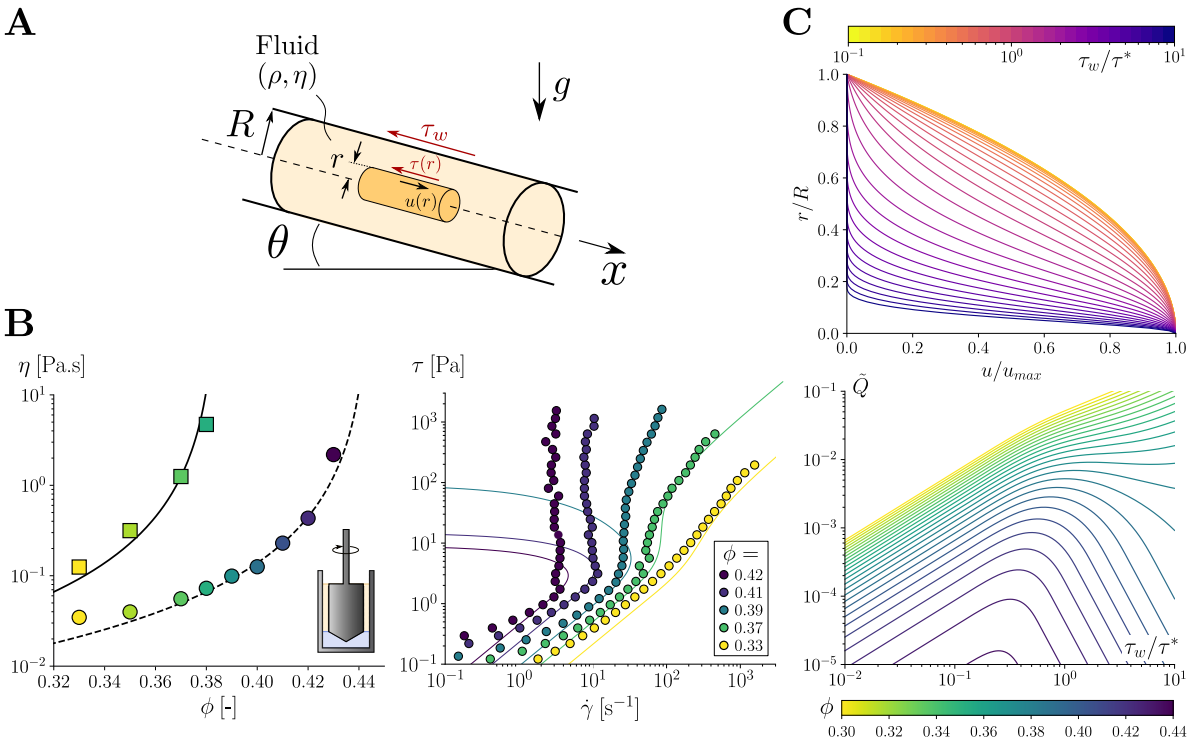

Fig. SI.2. (A) Force balance within the pipe cross-section. (B-left) Low-stress (circles) and high-stress (squares) viscosity branches. Dashed line: $\eta = \eta_S(\phi_0 - \phi)^{-2}$. Solid line: $\eta = \eta_S(\phi_1 - \phi)^{-2}$. (B-right) Shear stress τ versus shear rate $\dot{\gamma}$ for different volume fractions ϕ. Solid lines: fitted Wyart-Cates rheological laws. $\eta_S = 0.28$ mPa.s, $\phi_0 = 0.445$, $\phi_1 = 0.385$ and $\tau^* = 8.0$ Pa. (C-top) Normalized velocity profile, $u(r)/u_{\max}$ (Eq. [SI.4], with $u_{\max} = u(0)$), for different wall stress τ_w/τ^* and $\phi = 0.41$. (C-bottom) Normalized flow rate, $\tilde{Q} = \eta_s Q/R^3\tau^*$, versus τ_w/τ^*, for various ϕ. The parameters η_S, ϕ_0, ϕ_1 and τ^* are those obtained from the rheological measurements.

SI.4. Estimation of the cross-sectional profile of velocity in the frictional soliton

The opacity of the suspension restricts the observation of the flow to within a short distance λ from the wall (set by the laser penetration depth through the suspension). By calibrating the near-wall flow observations against the Poiseuille flow expected in the low-forcing regime, we estimate the typical slip velocity and the typical velocity gradient at the wall in the frictional soliton.

Two quantities are extracted from the movies: the mean flow velocity U_w within the near-wall observation depth λ, and variations of the flow velocity across the same depth (see variations in the slope of the spatio-temporal trajectories of the tracing particles in Fig. 3A-B of the main body of the paper). They are both obtained by measuring, for each of the two flow phases, the velocity component parallel to the pipe axis of 30 to 40 tracing particles randomly chosen within the observation depth.

Estimation of the near-wall observation distance. The near-wall observation distance λ is estimated from low-forcing flows, assuming a Poiseuille velocity profile. For a Poiseuille flow, the longitudinal velocity $u(r)$ follows a parabolic profile $u(r) = 2U(1 - r^2/R^2)$ relative to the radial coordinate r, with U the mean flow velocity and R the pipe radius. This means that the wall-distance $\lambda = R - r$ at which a given velocity U_w is observed follows

$$\frac{\lambda}{R} = 1 - \sqrt{1 - \frac{U_w}{2U}} \simeq \frac{U_w}{4U}\,. \qquad \text{[SI.5]}$$

From the velocity $U_w \approx 0.10U$ observed at low forcings ($\phi = 0.405$, $\langle\tau_w\rangle \approx 0.7\tau_c(\phi)$), one estimates the effective observation distance to the wall as $\lambda \approx 0.025R \approx 120\,\mu$m, or $\approx$ 5-10 cornstarch grain diameters of $\approx 15\,\mu$m, given $R = 5.15$ mm.

Estimation of the cross-sectional profile of velocity in the frictional soliton. The mean near-wall velocity in the frictional soliton is $U_w^{\rm FS} \approx 0.6U$ (for $\langle\tau_w\rangle \approx 2.9\tau_c(\phi)$), with U of the mean flow velocity in the pipe, as compared to $U_w \approx 0.10U$ for the laminar phases (all measurements are performed at $\phi = 0.405$). The relative variations in velocity across the observation depth is $\Delta U_w^{\rm FS}/U \equiv \sqrt{\langle u^2\rangle - (U_w^{\rm FS})^2}/U \approx 0.077$ in the soliton, as compared to $\Delta U_w/U \equiv \sqrt{\langle u^2\rangle - U_w^2}/U \approx 0.027$ for the laminar phases (independently of the level of applied stress, as long as $\langle\tau_w\rangle < \tau_c(\phi)$). Interpreting this variation as a proxi for the near-wall velocity gradient, i.e., $-\partial u/\partial r|_{r=R} \propto \Delta U_w/\lambda$ (since $\lambda/R \approx 0.025 \ll 1$), yields $-\partial u/\partial r|_{r=R} \approx 11U/R$ in the soliton, as compared to $-\partial u/\partial r|_{r=R} = 4U/R$ for the laminar phases (assuming, again, a Poiseuille velocity profile $u(r) = 2U(1 - r^2/R^2)$ in the laminar phases).

Altogether, these measurements suggests that the cross-sectional profile of velocity in the soliton is closer to a plug flow, with a significant slip velocity ($u^{\rm FS}(r = 0) \approx U_w^{\rm FS} + \lambda\partial u/\partial r|_{r=R} \approx 0.3U$) and a velocity gradient at the wall ($-\partial u/\partial r|_{r=R} \approx 11U/R$) of the same order of magnitude, though a few times larger, than in the laminar phases ($-\partial u/\partial r|_{r=R} = 4U/R$), as schematized in Fig. 3B of the main body of the paper.

SI.5. Contribution of diffusion to the transient growth of microscopic gas bubble in the frictional soliton

Microscopic gas bubbles, which are fortuitously trapped in the suspension, are found to expand, as the soliton passes, and to collapse, immediately after. This reflects the decrease of the liquid pressure within the soliton. In the main text, the magnitude of the pressure drop is estimated by assuming that the bubble growth is essentially due to the inflation of the gas that is initially inside the bubble. This demands that diffusive transport of gas from the solution to the bubble has a negligible contribution to the growth, which is what this appendix shows.

The radius $r(t)$ of a spherical bubble, growing by mass-limited diffusion in a non-moving supersaturated liquid, follows (7)

$$r^2(t) \approx r_0^2 + 2\frac{\Delta c}{\rho_g} Dt\,, \qquad \text{[SI.6]}$$

in the limit of both long times ($t \ll R^2/D$) and low supersaturation ($\Delta c/\rho_g \ll 1$), with r_0 the initial bubble radius, ρ_g the gas density inside the bubble, Δc the gas supersaturation of the liquid relative to the bubble condition expressed in kg/m^3, D the diffusion coefficient of the gas in the liquid, and t the time since $r = r_0$. For a sudden and large pressure drop, the supersaturation is (at most) equal to the density of gas dissolved in the liquid. Therefore, the supersaturation is also (at most) equal to the saturated density $c_{\text{sat,1 atm}}$, assuming that the liquid is close to saturation upstream of the soliton, where the pressure is $P \approx 1$ atm, consistently with the observation that bubble size is not varying rapidly, there.

This, together with Eq. [SI.6], implies that the diffusive growth time is approximately:

$$t \approx \frac{1}{2}\frac{\rho_g}{c_{\text{sat,1 atm}}}\frac{r^2 - r_0^2}{D}. \qquad \text{[SI.7]}$$

The initial bubble radius is $r_0 \approx 20\,\mu$m. The maximal radius $r(t)$ is (at least) twice as large. The gas density in the bubble is $\rho_g \approx 1.2\,$kg/m^3. Considering the contribution of nitrogen and oxygen, only, because they dominate the diffusive growth in air-equilibrated water, one has $c_{\text{sat,1 atm}} \approx 17\,$g/m^3 and $D \approx 2.2 \times 10^{-9}$ m^2/s.

Evaluating Eq. [SI.7] yields $t \approx 19\,$s (at least), which is much longer than the actual growth time $\sim l/(u+c) < 0.2\,$s. This comparison confirms that diffusive effects can be neglected in the sudden expansion of microscopic bubbles by the frictional soliton.

SI.6. Independence of flow rate saturation on the Reynolds number of the flow

Fig. SI.3 indicates that flow rate saturation (and the bifurcation of the flow from a single-phase low-forcing regime to a two-phase high-forcing regime) is observed at values of the Reynolds number of the flow ($Re \equiv \rho Q/\pi\eta_0 R$) varying by more than two orders of magnitude (including values much lower than one), as the particle volume fraction is varied.

The Reynolds number at saturation $Re_c = \rho Q_c/\pi\eta_0 R$ is actually selected by the shear-thickening onset condition given by Eq. [4] of the main body of the paper, i.e., $Q = Q_c \equiv \pi R^3 \tau_c(\phi)/4\eta_0$. This condition (dashed line in Fig. SI.3) is found to capture the saturated flow rate dependance on both the volume fraction ϕ (main graphics) and the pipe radius R (inset).

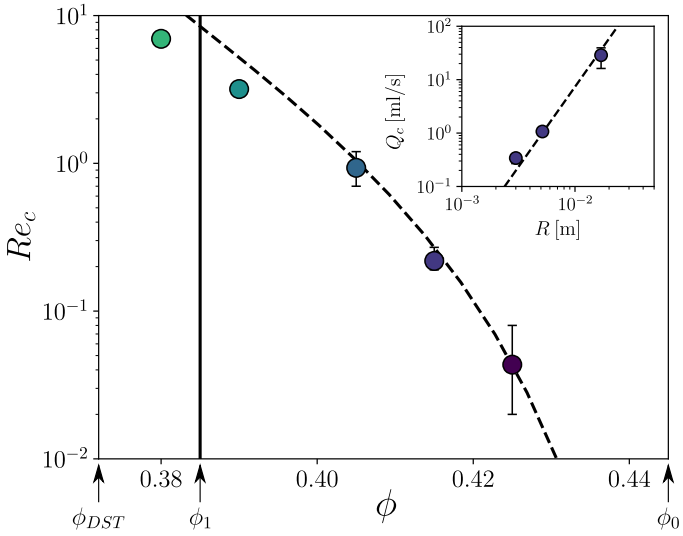

Fig. SI.3. (Main) Reynolds number $Re_c = \rho Q_c/\pi\eta_0 R$ at the onset of flow rate saturation (hence, of the high-forcing regime) vs particle volume fraction ($R = 5.15\,$mm, same data as in Fig. 2B of the main body of the paper). (Inset) Saturation flow rate Q_c vs pipe radius ($\phi = 0.415$). The dashed lines are the value expected from Eq. [4] of the main body of the paper, i.e., $Re_c = \rho Q_c/\pi\eta_0 R$, with $Q_c \equiv \pi R^3 \tau_c(\phi)/4\eta_0$.

SI.7. Sampling of the particle volume fraction at the pipe outlet

In order to verify whether the propagation of the frictional soliton is associated, or not, with a significant global redistribution of the particle volume fraction along the pipe, two additional experiments have been conducted, in the low- and high-forcing regimes, respectively, during which a few samples of suspension (~ 10 ml) are collected at the pipe outlet over the drainage duration. The particle volume fraction in each sample is determined by weighing the sample before and after it has been dried, under controlled conditions, in an oven.

Fig. SI.4 presents the evolution of the volume fraction collected at the pipe outlet ϕ_{out} for the low-forcing regime (○, $\langle\tau_w\rangle/\tau_c(\phi) \approx 0.7$) and the high-forcing regime (□, $\langle\tau_w\rangle/\tau_c(\phi) \approx 2.8$), for the same nominal (prepared) volume fraction of the suspension ($\phi = 0.405$). In both cases the collected volume fraction ϕ_{out} is found to remain undistinguishable (given the experimental accuracy of $\approx \pm 0.5\%$) from the nominal volume fraction ϕ.

This observation indicates that no significant global redistribution of the particle volume fraction along the pipe is associated with the frictional-soliton inception or propagation along the pipe. However, it does not permit to conclude about possibly significant redistribution of the particle volume fraction within the pipe cross-sections.

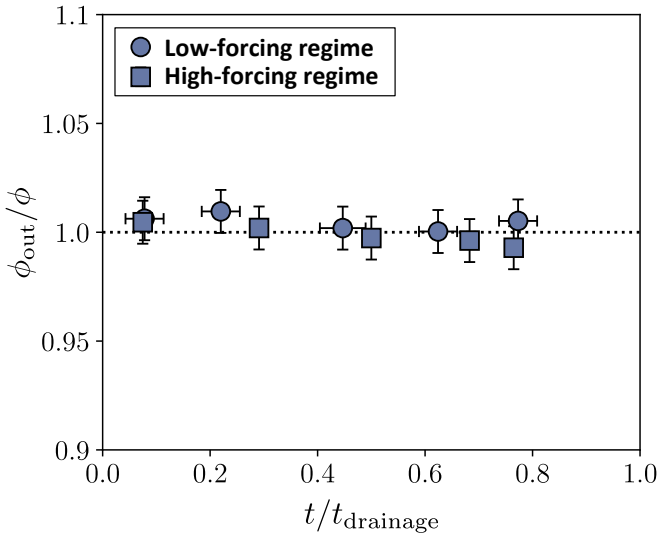

Fig. SI.4. Evolution of the suspension volume fraction ϕ_{out}, as collected at the pipe outlet, vs time. The nominal volume fraction is $\phi = 0.405$. t_{drainage} is the drainage time, at which the suspension free-surface reaches the pipe outlet and about 90% of the total suspension volume has drained. The symbol shape indicates the low-forcing regime (○, $\langle\tau_w\rangle/\tau_c(\phi) \approx 0.7$) or the high-forcing regime (□, $\langle\tau_w\rangle/\tau_c(\phi) \approx 2.8$). The pipe radius is $R = 5.15$ mm.

SI.8. Main characteristics of the effective rheology and of the frictional soliton for the different shear-thickening suspensions

Table SI.1 lists the low stress effective viscosity and the onset stress of discontinuous shear-thickening obtained from the rheological characterization of the cornstarch suspension and of the four other types of shear-thickening suspensions (A-D) presented in Fig. 6 of the main body of the paper. It also reports the measurements for the flow rate at saturation and the main characteristics of the frictional-soliton flow phase, together with the ranges of particle volume fractions and the range of mean wall stress at which they have been obtained.

			Cornstarch	(A) Potato starch	(B) Cassava starch	(C) Polystyrene spheres + cellulose	(D) Calcite + superplasticizer
Particle vol. fraction	ϕ	(–)	0.380-0.425	0.420	0.448	0.595	0.534
Rheological param.	η_0	(Pa.s)	0.07-0.7	0.20±0.01	0.13±0.01	0.45±0.03	0.3±0.2
	τ_c	(Pa)	2.6-7.6	2.1±0.1	2.8±0.2	23.9±2	0.8±0.3
Mean wall stress	$\langle\tau_w\rangle/\tau_c$	(–)	1.0-31.5	1.3-7.3	2.7-10.9	3.2-5.8	52±31
Saturation flow rate	$Q_c/\frac{\pi R^3\tau_c}{4\eta_0}$	(–)	0.8±0.3	1.2±0.1	1.0±0.1	2.6±0.7	4.6±2.1
Frictional-soliton characteristics	$l/2R$	(–)	1.5±0.5	0.9±0.5	1.3±0.3	0.9±0.3	1.1±0.1
	c/U	(–)	1.5±1.0	5.6±1.4	2.5±1.4	0.8±0.2	6.2±0.6
	U_w^{FS}/U_w	(–)	8.2±4.6	5.7±0.4	9.4±1.2	2.0±0.2	8.3±1.0

Table SI.1. Values separated by an hyphen (-) stand for a range of variation. Values separated by a ± symbol indicate the average and the standard deviation over all experiments performed in the range of variation.

Reference

1. G Bossis, Y Grasselli, and O Volkova. Capillary flow of a suspension in the presence of discontinuous shear thickening. *Rheol. Acta*, 61:1–12, 2022.
2. R O'Neill, J Royer, and W Poon. Liquid migration in shear thickening suspensions flowing through constrictions. *Phys. Rev. Lett.*, 123:128002, 2019.
3. M Wyart and M Cates. Discontinuous shear thickening without inertia in dense non-Brownian suspensions. *Phys. Rev. Lett.*, 112:098302, 2014.
4. J Goddard. Material instability in complex fluids. *Ann. Rev. Fluid Mech.*, 35:113–33, 2003.
5. T Divoux, A Fardin, S Manneville, and S Lerouge. Shear banding of complex fluids. *Ann. Rev. Fluid Mech.*, 48:81–103, 2016.
6. F Rocha, Y Forterre, B Metzger, and H Lhuissier. Drag of a shear-thickening suspension on a rotating cylinder. *J. Fluid Mech.*, 970:A35–19, 2023.
7. P Epstein and M Plesset. On the stability of gas bubbles in liquid-gas solutions. *J. Chem. Phys.*, 18:1505–09, 1950.